aerospace

MDPI

Article

Experimental Characterization of C–C Composite Destruction Under Impact of High Thermal Flux in Atmosphere and Hypersonic Airflow

Ryan Bencivengo [1], Alin Ilie Stoica [1], Sergey B. Leonov [1,*] and Richard Gulotty [2]

[1] Department of Aerospace and Mechanical Engineering, University of Notre Dame, Notre Dame, IN 46556, USA; rbencive@nd.edu (R.B.); astoica@nd.edu (A.I.S.)
[2] Honeywell International Inc., 50 E Algonquin Rd, Des Plaines, IL 60017, USA; richard.gulotty@honeywell.com
* Correspondence: sleonov@nd.edu

Abstract: Hypersonic flight in the atmosphere is associated with high thermal flux impacting the vehicle surface. The nose, leading edges, and some elements of the engine typically require the implementation of highly refractory materials or an active thermal protection system to maintain structural stability during the vehicle mission. Carbon–carbon (C–C) composites are commonly considered for the application thanks to their unique thermal and mechanical properties. However, C–C composites' ablation and oxidation under long cruise flights at high speeds (Mach number > 5) are the limiting factors for their application. In this paper, the results of an experimental study of C–C composite thermal ablation and oxidation with test article surface temperatures up to 2000 K are presented. The tests were performed under atmospheric conditions and hypersonic flow in the ND_ArcJet facility at the University of Notre Dame. The test articles were preheated with CW laser radiation and then exposed to M = 6 flow at stagnation pressures up to 14 bar. It was found that C–C composite oxidation and mechanical erosion rates are significantly increased in hypersonic airflow compared to those at ambient conditions and nitrogen M = 6 flow. Compared to atmospheric air, mass loss occurred at a rate of 1.5 orders of magnitude faster for M = 6 airflow. During high-speed flow conditions, rapid chemical oxidation and the mechanical destruction of weakened C-fibers likely cause the accelerated degradation of C–C composite material. In this study, a post-mortem microscopic analysis of the morphology of the C–C surface is used to explain the physical processes of the material destruction.

Keywords: carbon–carbon (C–C) composites; hypersonic airflow; mechanical destruction; thermal ablation; oxidation

Academic Editors: Ikhyun Kim and Yosheph Yang

Received: 30 November 2024
Revised: 10 January 2025
Accepted: 10 January 2025
Published: 11 January 2025

Citation: Bencivengo, R.; Stoica, A.I.; Leonov, S.B.; Gulotty, R. Experimental Characterization of C–C Composite Destruction Under Impact of High Thermal Flux in Atmosphere and Hypersonic Airflow. *Aerospace* **2025**, *12*, 43. https://doi.org/10.3390/aerospace12010043

1. Introduction

Vehicles that re-enter Earth's atmosphere or vehicles that fly at hypersonic velocities in the atmosphere experience high thermal and mechanical loads as a result of the air compression (stagnation temperature $T_0 > 2000$ K and stagnation pressure $P_0 > 3$ MPa). To overcome this problem, highly refractory materials or active thermal protection systems are utilized for the construction of hypersonic vehicles. Thermal protection systems are typically heavy, expensive, and time-consuming to design. In many cases, the application of refractory materials is more practical, but is challenging because the properties of the materials dictate the operating parameters of the vehicle. C–C composites are a class of prospective materials for hypersonic vehicle construction. The current study provides insight into the physical

mechanisms of C–C composites destruction under harsh environmental conditions relevant to hypersonic flight.

The design of vehicles capable of flying in the hypersonic regime has been under extensive development for many decades [1]. A key problem in the advance of hypersonic vehicles is managing the intense thermal heat flux and temperature spikes that occur because of air compression over the vehicle surface [2,3]. Additionally, for vehicles utilizing air breathing propulsion systems, strict limitations are applied to components within the engine as high thermal loads are encountered. This requires the implementation of systems designed for extreme heat flux protection. Most affected by high heat fluxes are the nose tip and the leading edges, which oftentimes have quite small surface areas compared to the vehicle total surface. Due to these constraints, the ability for active cooling of the leading edges becomes challenging [4]. A potential solution to this problem is the use of refractory materials possessing high temperature melting/ablation points and high thermal conductivities, which would allow the material to spread and dissipate heat efficiently [5,6]. The latter design challenge requires that certain components of the vehicle, such as the leading edge or heat shield, be constructed of materials that can withstand extremely high temperatures of 2000 K or greater [7,8] without melting while also maintaining high mechanical strength for the given flight conditions.

Conventional aerospace materials, such as most metal alloys or their derivatives, have lower melting points than what is required for hypersonic flight or are prohibitively heavy. Ultra-high temperature ceramics may be an alternative thanks to their refractory properties [6,9], but they are typically brittle and difficult to machine efficiently. Also, surface cracks (caused by thermal shocks) may occur after installation or during flight. Therefore, though the most conventional materials may provide ready-made technology for this application, they may not fulfill all the requirements, such as efficient withstanding of high heat flux going into the vehicle, which may cause serious problems for extended flights.

Other types of materials, such as C–C composites, have been in research and development for many years for various applications in the aeronautics industry, including hypersonic flight [10]. However, limited research has been performed to study the behavior of these materials at high time-variable thermal fluxes, when surface temperatures exceed 2000 K, not to mention 2000 K [11] under high-speed flow. Several computational efforts have been performed to study the oxidation rate and mechanisms of carbon–carbon composite destruction under hypersonic flight conditions [12]. A series of studies were published related to C–C composite nozzle material recession [13–15]. A few experimental studies have been completed and published regarding the C–C composite behavior at high temperature, including oxidation, which can be seen in references [16–18]. The use of C–C composites for hypersonic flight becomes of high interest as this material had showed highly promising thermal properties combined with relatively strong mechanical characteristics [19] such as: low density (1.60–1.98 g/cm^3), low coefficient of thermal expansion (-0.85 to 1.1×10^{-6} 1/K), high modulus of elasticity (200 GPa), relatively high thermal conductivity (4–35 W/(m-K)), and the retaining of mechanical properties at temperatures up to 2300 K in inert environments. The most commonly considered engineering applications include the implementation of C–C composites in the construction of hypersonic vehicles leading edges [7,19], air inlet cowl leaps, nozzles, fins, and other surfaces experiencing high thermal loads.

In the hypersonic flow regime, the main sources of heat transfer/exchange for materials at high thermal loads are axial and radial thermal conduction, gas convection, radiation, ablation, and chemical reactions. The emissivity of the C–C composite is generally high, close to 0.86 at 1990 K, which makes it efficient at removing heat when considering radi-

ation [20]. The C–C composite materials have multiple ways of removing heat from the system at the cost of replacement after each flight.

Ablation, which is to be determined in this work, is also a significant contributor to the heat absorbance at $T_{surface}$ > 2500 K [21], or even lower temperatures as it is hypothesized in this work. The most significant issue facing the implementation of C–C composites in thermal protection systems is oxidation in a chemically active environment, such as atmospheric air at high temperatures. For cruise flights, oxidation is the major limiting factor. With increasingly more extreme hypersonic environments, two protection approaches are being developed: (1) deposition of high-temperature protective coatings, and (2) modification of the carbon–carbon matrix. An example of C–C matrix modification would be the addition of HfB_2 to improve oxidation resistance in air. Ablation processes may also be reduced at low heat fluxes such as 2.4 MW/m^2 or lower. However, cracking of the protective layer is a limiting factor at heat fluxes greater than 4.2 MW/m^2 [22].

Since flight testing is highly time- and funds-consuming, and simulations of complex composition and shapes are challenging and inaccurate without extensive validation, intensive and robust experimental ground testing is of high demand for the collection of reliable data and to properly validate the results of computational modeling. In the case of ground testing, there is still limited availability of measured data for the C–C composite in hypersonic environments, which may be reproduced to obtain consistent databases. Note, that in general, there is no one single method of ground testing which can properly simulate the hypersonic environment in all relevant aspects [23].

In environments such as air with high heat flux and temperature, mass ablation rates rapidly increase with increasing exposure time while the linear erosion rate demonstrates a bilinear response decrease after an initial rise [24]. This is due to the machining process of the articles causing fiber fragmentation, which weakens the fiber and matrix interfaces, resulting in an initial surge in mass loss due to ablation for the first test run of a new article. Furthermore, long fibers have better resistance to the shear forces generated by flows like plasma streams [24]. The oxidation process of the carbon fibers leads to a pointy morphology. The interface between the fiber and the matrix oxidizes at a much higher rate when compared to the core of the fiber. For long exposure times, at temperatures lower than 1100 K the chemical reaction rate is the governing factor since the oxidation is uniform throughout the articles. However, for higher temperatures, greater than 1400 K, the oxidation of the C–C composite occurs prevalently along the edges. This shows that gas phase diffusion significantly contributes to the oxidation process. Under a microscopic view, there are oxidation voids in the articles exposed to high temperatures either in a furnace or arc jet flow. However, these oxidation voids are distinguishable from imperfections due to machining or processing because oxidation voids are only present on pointy fibers with no surrounding matrix, and on delineated fibers along the edge [25]. These results were observed under electron microscopy scanning for raw C–C articles. Adjacent to the fibers, there are areas of increased local stress in the matrix, which crack gradually under oxidation, allowing oxygen diffusion into the matrix/fibers [26]. Furthermore, for the C–C composites made via the Chemical Vapor Infiltration (CVI) process, the material structure consists of areas with increased porosity and noticeable density gradients in the C–C material volume causing the recession rate to be dependent on the porosity and density of the raw material [27].

The objective of this study is to characterize and quantify the process of C–C composite destruction under high-temperature conditions, including the mass loss as the result of thermal ablation and oxidation in atmosphere and at hypersonic flow exposure. The paper poses the detailed experimental results relevant to the destruction of a C–C composite under various conditions. Destruction is assessed by the mass loss and the surface morphology

modification. Most of the analysis was focused on the material destruction under M = 6 hypersonic flow at a controlled temperature of the test article surface above 1000 K. Both the physical mechanisms of the test-article material recession and a quantification of the rates of recession were analyzed. A post-mortem microscopic analysis of the morphology of the C–C surface is used to explain the physical processes of the material destruction.

2. Materials and Methods

2.1. Heat Transfer Mechanisms

The ablation and oxidation processes of the test article exposed at hypersonic flight conditions are of major interest. To provide consistent and reliable testing, the test article, in the form of a blunt body, is placed in three environmental conditions: (1) atmospheric conditions with surrounding still air and laser exposure centered to the front face of the test article, (2) vacuum conditions with laser exposure, and (3) M = 6 flow conditions with laser exposure. Laser exposure was set at different power ratings to generate up to 10.6 MW/m^2 for 360 s of exposure time and was consistent within each test. The beam diameter of the high-power laser is 8 mm and can be expanded when needed. The heat transfer problem is displayed in Figure 1 for each test type. This procedure is mainly focused on providing insights on mass loss dynamics with respect to measured surface and internal temperature and determining ablation and oxidation rates.

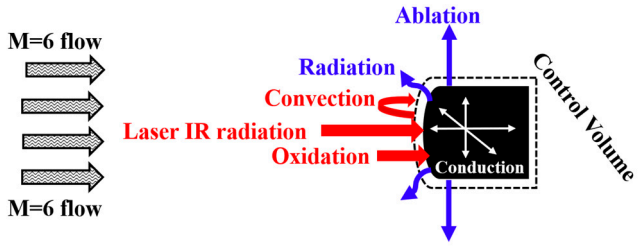

Figure 1. Schematics of the test article thermal balance under hypersonic M = 6 air flow. For atmospheric testing conditions, convection would cool down the article, whereas, under vacuum conditions, convection and oxidation do not occur.

The means of heat transfer shown in Figure 1 illustrate how the article is heated and cools down. A control volume drawn around the article describes the general thermal balance equation for the test article in airflow, as shown in Figure 1 (the sign of the heat flux q depends on the gas and surface temperatures, see below) is provided in Equation (1).

$$q_{projected\ laser} + q_{convection} + q_{oxidation} - q_{radiation} - q_{ablation} - q_{conduction} = \rho c_p \frac{\partial T}{\partial t} \quad (1)$$

In Equation (1), the positive terms refer to heat entering the control volume, while the negative terms provide heat exiting the control volume. The heating of the article is provided by the continuous-wave laser beam projected on the front face of the article, the convective heat transfer is realized with the hypersonic flow within the compression and boundary layer, and conduction is through the article with anisotropic thermal properties (varying thermal conductivity axially and radially). The hot surface of the article will radiate heat out of the control volume. The ablation of the C–C material provides a means of cooling, while oxidation adds more heat to the article. The conductive, convective, and radiative heat transfers can be described in a conventional way, see below for the basic equations; however, the ablation and oxidation require further attention.

The projected heat flux coming from the laser and going into the control volume is simply calculated by using the power rating of the laser equipment used for the run divided by the surface area of the beam projection on the article front side. The total heat flux that is

projected onto the article would be at its maximum 10.6 MW/m^2. Taking into account 8% light reflection from the optical window and about 96% of the light absorption by the test article surface, actual total heat flux is about 9.4 MW/m^2 at the laser maximum power. Note that for a real cruise flight, the calculated convective heating would be up to 50 MW/m^2 and a temperature of 2400 K at the surface of the leading edge of the vehicle travelling at M = 6 cruise speeds. While the test article is being exposed to the laser radiation, thermal conduction occurs throughout the article in the radial, angular, and axial directions, (r,ϕ,z). C–C materials have anisotropic thermal properties, and thermal conductivity can then be modeled as dependent on the direction, k(r,ϕ,z), and an equation for thermal conductivity can be written in cylindrical coordinates as shown in Equation (2a), which, in the one-dimensional case, could be simplified to Equation (2b). Convective heat transfer from high enthalpy hypersonic airflow can be estimated by Equation (3a), where for hypersonic flow the free stream enthalpy is $h_\infty >> h_w$ and therefore the enthalpy ratio, h_w/h_∞, approaches 0, ρ is the density of gas at the stagnation point, and $R_n = d/2$ is the leading-edge radius and d is the diameter of the blunt body. This shows the need of either high-enthalpy flow (arcjet, for example) or laser preheating of the article to replicate the thermal conditions of the hypersonic flight. Under the current conditions with laser preheating, the processes of oxidation, ablation, and thermal shocks are simulated by a cold hypersonic flow impinging the test article for a short duration when the surface temperature is high and relatively stable. The forced convective heat transfer between the preheated article and the hypersonic flow can be estimated by Equation (3b), where h is the convective heat transfer coefficient, which is a function of Reynolds, Re, and Prandtl, Pr, numbers (used to calculate Nusselt number, Nu). For the current test conditions (estimated values $Re_d \approx 10^6$; Pr = 0.715 for air; $Nu_d \approx 600$; h ≈ 2.4 × 10^3 W/m^2 K), the negative convective heat flux is estimated in a range of $q_{convection} = -2$ MW/m^2 to -4 MW/m^2 that is less in magnitude than the laser heating thermal flux. Radiative cooling of the article is a main source for heat transfer under high temperature conditions. For any given point on the surface of the article and neglecting the roughness and the shrinking of the article, the radiative cooling can be described by Equation (4), where σ is the Stefan–Boltzmann constant and ε is the emissivity of the test article surface.

$$\frac{1}{r}\frac{\partial T}{\partial t}\left(rk(r)\frac{\partial T}{\partial r}\right)+\frac{1}{r^2}\frac{\partial}{\partial \phi}\left(k(\phi)\frac{\partial T}{\partial \phi}\right)+\frac{\partial}{\partial z}\left(k(z)\frac{\partial T}{\partial z}\right)=\rho c_p\frac{\partial T}{\partial t}, \tag{2a}$$

$$q_{conduction}=-k\frac{dT}{dz} \tag{2b}$$

$$q_{convection}=1.63\times10^{-4}\left(\frac{\rho}{R_n}\right)^{\frac{1}{2}}\left(1-\frac{h_w}{h_\infty}\right) \tag{3a}$$

$$q_{convection}=-h\cdot\left(T_{surf}-T_{flow}\right),\ h=Nu_d\cdot\frac{k}{d},\ Nu_d=2+0.4\cdot Re_d^{1/2}\cdot Pr^{1/3} \tag{3b}$$

$$q_{radiation\ at\ point(r,\phi,z)}=\varepsilon\sigma T^4_{surf(r,\phi,z)} \tag{4}$$

$$q_{ablation}=A_b\cdot\frac{dm_{ablation}}{dt} \tag{5}$$

The ablation of the material of the test article can be described using Equation (5), where $A_b$represents ablation heat factor, similar to latent heat, while $dm_{ablation}/dt$ is the mass loss due to ablation. One of the sources of heat addition is the oxidation process. The carbon in the C–C composite chemically reacts with the O_2 in the working gas. The main

products of carbon oxidation are CO and CO_2 [16] and the heterogenous global chemical reactions are described in Equation (6) through Equation (8):

$$C_{(s)} + O_2 \rightarrow CO_2 \; with \; \Delta G^\circ = -399.13 + 2.48 \times 10^{-3} \; T \; (\mathrm{kJ/mol}) \; at \; T < 500 \; ^\circ\mathrm{C} \quad (6)$$

$$C_{(s)} + \left(\frac{1}{2}\right) O_2 \rightarrow CO \; with \; \Delta G^\circ = -220.9 + 0.179 \; T \; (\mathrm{kJ/mol}) \; at \; T > 500 \; ^\circ\mathrm{C} \quad (7)$$

$$C_{(s)} + CO_2 \leftrightarrow 2CO \; with \; \Delta G^\circ = -172.2 + 0.177 \; T \; (\mathrm{kJ/mol}) \quad (8)$$

The volumetric oxidation process is defined by the following global reaction:

$$C_{2(g)} + O_2 \rightarrow 2CO \; with \; \Delta G^\circ = -937.0 + 0.1912 \; T \; (\mathrm{kJ/mol}) \quad (9)$$

$$CO + (1/2)O_2 \rightarrow CO_2 \; with \; \Delta G^\circ = -565.4 - 0.174 \; T \; (\mathrm{kJ/mol}) \; at \; T > 500 \; ^\circ\mathrm{C} \quad (10)$$

where ΔG° is the Gibbs free energy change. The heat flux generated by the oxidation reaction may then be described as shown in Equation (11):

$$q_{oxidation} = F \times \frac{dm_{oxidation}}{dt}, \quad (11)$$

where F represents the factor that accounts for a portion of the heat flux produced by oxidation going into the control volume, and $dm_{oxidation}/dt$ is the mass loss rate due to oxidation.

After simplifications, the analysis of Equations (1)–(5) allows for the estimation of a few numbers important for the test planning, such as a characteristic time of the test model heating by laser irradiation, t_{heat} = 30–50 s; maximum achievable temperature at predefined laser power when $T_{surface}$ is lower than 2000 K; and the cooling rate in the high-speed cold flow, which is greater than 200 K/s. The result of a simplified analysis of the contribution of the chemical reactions, Equations (6)–(10), in the thermal balance is briefly discussed in Section 3.3.

2.2. Experimental Test Setup and Conditions

The ground test facility ND_ArcJet schematics are shown in Figure 2. The ND_ArcJet is a short-duration arc-heated hypersonic wind tunnel at the University of Notre Dame capable of simulating the high temperature conditions of hypersonic flight. The facility became operational in 2012 and offers a unique test platform for experimental studies of high enthalpy phenomena in hypersonic flows, non-equilibrium plasma-structure interactions, materials testing, and scramjet turbulent combustion problems. The flow parameters are as follows: flow Mach numbers M = 4.5, 6 and 9; stagnation temperatures T_0 = 300–6000 K; total gas pressures P_0 = 1–40 bar; flow run time up to 1 s. A significant drawback of the testing at the ND_ArcJet is a relatively short time of the hypersonic flow exposure. To overcome this, the test article was preheated by a near-IR CW laser up to a predefined surface temperature from $T_{surface}$ = 300 to 2000 K. For the article preheating, a multi-mode ytterbium fiber laser YLR-500-MM-AC-Y14 (IPG Photononics, Oxford, MA, USA), 500 W CW power was utilized. For the purpose of the described testing, the facility is equipped with high-speed filtered imaging cameras, an IR camera (surface temperature monitoring), fast pressure sensors, and a high definition schlieren system.

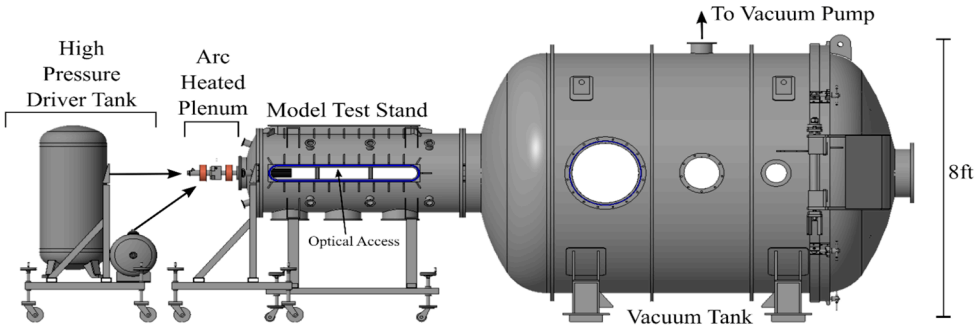

Figure 2. ND_ArcJet test facility with capabilities of M = 6 high enthalpy flow of various gases.

Ground testing of the materials at hypersonic conditions can be performed using various shapes of the test article. The basic shapes include a conic tip, leading edge (wedge), blunt body, acreage, and their combinations. In terms of the reproducibility of results and the validation of simulations, the most representative shape relevant to ground testing and which provides more accurate results of the capability of the material is the blunt body. The data could be then reduced to other shapes once a database for the specific C–C shape is available. Three-directional needled felt PAN-based carbon fiber reinforced carbon matrix commercial composites were provided by Honeywell Aircraft Landing Systems, similar to those provided in previous investigations [28,29]. The C–C material is graphitized via heat treatment after Chemical Vapor Infiltration (CVI) densification. The shape and dimensions of the test article are based primarily on the capabilities and efficiency of measurements. The article is shaped in a blunt body geometry, see Figures 3 and 5, and is hollow with 7.6 mm thickness of solid C–C material along and on the front end with the following dimensions: outer diameter of 25.4 mm and inner diameter of 9.7 mm to provide access for a K-type thermocouple. The front end is 9.5 mm thick with solid C–C material. The thermocouple is initially located on the interior surface of the front end, 9.5 mm away from the flow stagnation point where the laser beam projects the heat flux. The entire test article is expected to shrink as it is exposed to heat flux and consequently ablation and oxidation occur. Two orifices of 1.5 mm diameter are drilled throughout the body to provide access for Alumina-based pins, which hold the article in place in the test stand. Heat transfer via the pins interface would be neglected due to the small footprint compared to the entire article surface and very low thermal conductivity of the pins. Multiple test articles of the same size and features were machined and used for the testing. Machining of the test articles was made such that the main fiber orientation is either parallel or perpendicular to the front face surface, and thus parallel/perpendicular to the hypersonic flow. This paper is specifically focused on the uncoated "parallel" article mass loss dynamics. Material properties considered for this study were similar to [19] such as low density (1.60–1.98 g/cm^3), low coefficient of thermal expansion (-0.85 to 1.1×10^{-6} 1/K), high modulus of elasticity (200 GPa), relatively high thermal conductivity (4–35 W/(m-K)), and the retaining of mechanical properties at temperatures up to 2300 K in inert environments.

The experimental procedure of any test starts with measuring the mass of the test article beforehand. The test article is then placed inside the wind tunnel, as shown in Figure 3, 100 mm away from the exit plane of the M = 6 nozzle. The continuous wave laser, IPG Photonics YLR-500-AC S/N PLMP322-1728 (IPG Photonics, Oxford, MA, USA), is then set at the predefined power, ranging from 0 to 534 W, where the latter represents the maximum power rating for the equipment, with an 8 mm beam, and the emission in the infrared spectrum $\lambda = 1.06$ µm. The duration of laser exposure is set to 360 s where for any given heat flux, the maximum surface temperature is reached at 330 s.

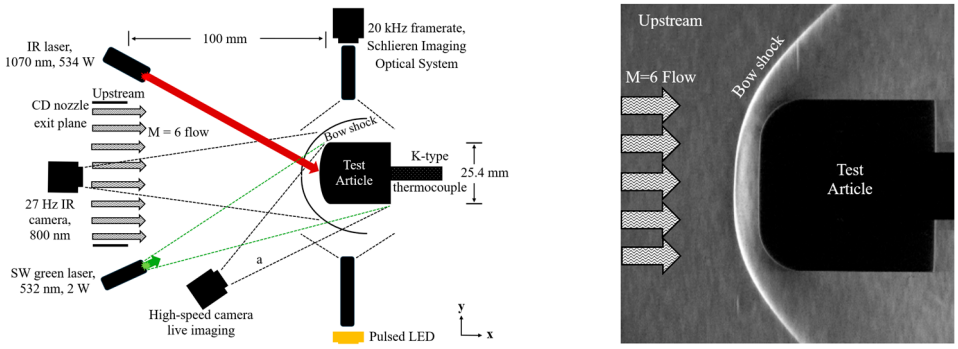

Figure 3. (**a**) Top view schematics of test setup for M = 6 flow test with the drawing not to real scale; (**b**) schlieren image of the test article in M = 6 flow.

An Optris™ Xi 1M InfraRed camera (Optris GmH & Co., Berlin, Germany), spectral range around $\lambda = 0.8$ µm, is then adjusted and triggered to record surface temperature with a sampling frequency of 30 Hz and 100 × 180 pixel resolution. The internal temperature of the article is measured with a K-type thermocouple, using room temperature as a reference point. An oscilloscope set at 4 kHz sampling frequency records the internal temperature signal from the thermocouple. Both the IR camera and thermocouple are triggered synchronously when laser emission is started. Laser emission, set at different power ratings as described above, is projected onto the test article, with the point of impingement being centered on the front face. The laser power rating remains constant throughout the entire run. When the vacuum test is performed, the wind tunnel test section is first pumped out to a total pressure of less than 1 mbar. Once vacuum conditions are reached, laser emission is started, with the longest exposure time being 360 s. When the M = 6 test is performed, the wind tunnel is first pumped out to vacuum, then the article is exposed to laser emission and allowed to reach a steady state temperature at the surface and interior. With the laser still on, M = 6 flow of either air or nitrogen is released with a steady-state flow duration of 1 s. For atmospheric room temperature and pressure testing, the article is allowed to cool down back to room temperature for 930 s after 360 s of laser exposure time. For vacuum and M = 6 flow tests, the test article is also cooled down for 930 s after 360 s of laser exposure time to allow the temperature of the article to come back to the reference point and reduce any oxidation from bringing the tunnel back to atmospheric pressure. Mass flow rate of the M = 6 flow is controlled by changing the driver tank pressure (higher pressure for larger mass flow).

The test arrangement for the M = 6 flow is shown in Figure 3a. The working gas for the hypersonic flow is provided by industrial grade gas stored in compressed gas cylinders. The same components, such as the laser, test article shape and features, and measurement techniques, are used for atmospheric testing and vacuum conditions with no flow. The test article mass is measured before each test. Then, after the test article is naturally cooled, the article is weighed again, and the mass measurement is recorded. For M = 6 flow testing, a schlieren visualization was also taken for a few runs at cold flow (laser off) and hot conditions (laser on) at 20 kHz framerate. This system is triggered to record images only when the M = 6 wind tunnel is triggered. The schlieren images were also utilized to confirm that the flow is steady for 1 s, and that it is ideally expanded at the exit of the converging–diverging nozzle and for a distance of, at least, 1250 mm. An example of the schlieren images is shown in Figure 3b. An example of mass loss data processing according to the characterization in Figure 4 for hypersonic flow runs is shown in Table 1.

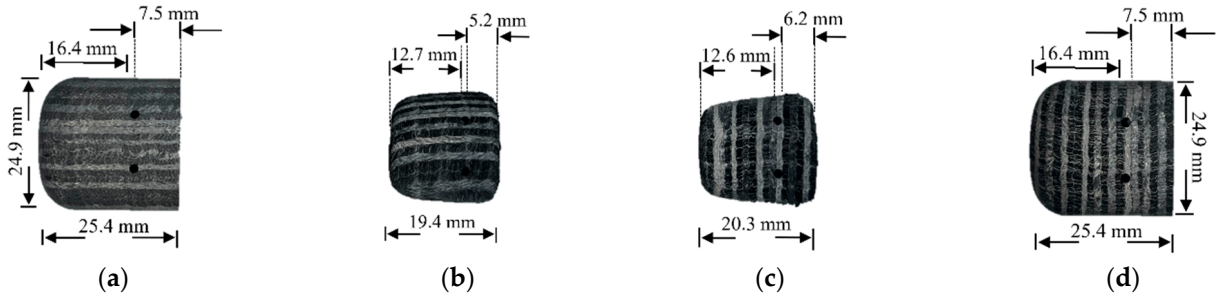

Figure 4. Article images of both machining orientations: (**a**) parallel new; (**b**) parallel decommissioned (after at least 3600 s of cumulative laser exposure); (**c**) perpendicular decommissioned; and (**d**) perpendicular new.

Table 1. Relevant data from M = 6 flow experiments.

Parameter	Run 1	Run 2	Run 3
Flow Gas Employed	Air	Air	Nitrogen
Stagnation Pressure (bar)	6.9	14	6.9
Flow Rate through nozzle (kg/s)	0.073	0.146	0.073
Total Mass Loss Rate (mg/s)	88.5	93.5	31.2
Mass Loss Rate due to Oxidation (mg/s)	58.2	61.4	0.00
Mass Loss Rate due to Ablation and Mechanical Erosion (mg/s)	30.3	32.1	31.2

Live images of the article undergoing testing were achieved using a Phantom v2512 camera, as shown in Figure 3a. A 550 nm shortpass filter and a hot glass IR filter were placed in front of the camera lens to block the article's blackbody radiation and laser infrared radiation reflection. A high-resolution optical lens with a 200 mm focal length was used on the camera for zoomed imaging at the required working distance. Additionally, two teleconverter lenses were used, one 2× and one 1.4× to provide enhanced zooming on the face of the article. Due to the required short exposure time of the camera, the test article was illuminated in 532 nm green light using a SW laser, synced with the camera sampling frequency, with a maximum power of 2 W, positioned outside of the tunnel. The green laser was positioned to illuminate the portion of the article being imaged.

The specific characteristics of material destruction studied include an overall quantification of material mass loss and a specific qualitative analysis of carbon fiber and carbon matrix morphological alteration. The testing under different environments and corresponding analyses using high-framerate footage, mass loss quantification, and scanning electron microscopy allows for the determination of various morphological changes, such as the inherent structure and the shape of the internal carbon fibers, to be attributed to specific mechanisms, such as mechanical erosion, rapid oxidation, etc. It should be noted that fracture toughness testing of the bulk material is out of scope of this paper.

2.3. Calibration of Instrumentation

Calibration of the test instrumentation includes calibrating the lab grade scale according to specs for every day of testing with a precise 1000 mg weight provided by the manufacturer, and assuring the scale sits on a flat, level surface. Continuous use of the scale proved that there is a standard deviation of mass measurements of ±1.0 mg, and for the mass loss rates it is ±0.1 mg/s. The thermocouple is calibrated to measure internal temperature of the test article with room temperature as a reference point and was set at 4000 samples/s recording using the oscilloscope. The IR camera is calibrated using

software provided by the manufacturer and by installing a spectral filter to block any reflection from the lasers. The IR camera temperature data was initially compared to optical spectrometer data obtained for the same laser exposure conditions and the temperatures were confirmed to be consistent. A formal error on the temperature readout indicated by IR video is ±1% for a surface temperature lower than 1800 K and ±2% for temperatures greater than 1800 K, but that does not take into account the temperature variation over the surface on a microscale.

Mass loss measurements for the hypersonic testing conditions imply several calibration tests need to be performed and considered for any mass changes. The calibration tests helped to quantify mass changes due to equipment/experimental procedure rather than the thermal ablation and oxidation mechanisms. The following calibration tests, although with minimal mass losses, were accounted for: handling of article during installation/removal (friction), vacuum conditions with no heat flux exposure (fracture of cold fibers caused by bringing the test section from atmospheric pressure to vacuum, vacuum duration, and repressurizing after testing completion), any oxidation due to residual air in the tunnel after bringing to vacuum, and any losses caused by cold M = 6 flow (breaking of fibers when the article is not exposed to the laser but only to hypersonic airflow). The latter would be used for comparison to a hot article under M = 6 airflow to demonstrate that the ablation and oxidation is driven by the high heat flux and consequently the high temperature. The mass loss caused by ablation is measured by performing the following tests: vacuum and laser exposure to the article (thermal stress causing weakening of fibers), and M = 6 N_2 flow causing mechanical erosion. The ablation–oxidation measurement is performed with the article being exposed to heat flux generated by the laser, and the highly compressed airflow released when the article is held at constant maximum temperature, causing oxidation.

The assumptions made were as follows: reference temperature to be room temperature, and articles being considered blackbodies with emissivity and absorptivity close to 1. For hypersonic conditions, mass loss dynamics were categorized in three classes: calibration (mass loss due to the testing procedure and not caused by ablation/oxidation), ablation mass loss, and ablation–oxidation mass loss. These calibration and measurement tests offer the possibility of characterizing the mass loss dynamics quantitatively. For instance, one performs an M = 6 test with air as the working gas and a mass loss number is obtained. Performing a test with N_2 or Ar should result in a different mass loss quantity due to the lack of the oxidation process, but ablation due to very high heat flux provided by the laser and the hypersonic flow conditions would still provide the ablation mechanism at the surface level.

3. Results

3.1. Ablation/Oxidation Measurements at Atmospheric Conditions

Heat flux played a substantial role in the mass loss rate of the test articles under atmospheric conditions. The total energy deposited into the test article is a function of the output power of the laser and the total run time of the test. To vary the total energy deposited into the test article, either the laser output power, or the run time can be varied. Tests were performed to achieve an identical total energy deposition, but with differing run times and differing laser output powers. The cases with higher laser output powers had a notably higher mass loss rate, indicating that the rate of energy delivery, namely the heat flux on the test article surface, has a significantly more impactful effect on the thermal response and the mass loss behavior of the material when compared to simple run time. The reason for this is likely due to a combination of a few factors. First, a higher surface temperature on the test article leads to faster rates of oxidation of the test article. As indicated in Equations (7) and (8), as the temperature on the test article increases, ΔG°

becomes increasingly negative, which makes the direct oxidation reaction, Equation (6), and volumetric oxidation more thermodynamically favorable. Additionally, rapid temperature increases because of higher heat fluxes can cause intense thermal gradients within the material, potentially leading to points of structural weaknesses induced by thermal stress. The temperature gradient may achieve significant magnitude, such as when the maximal outer surface temperature of 1770 K and internal temperature at the location of the thermocouple of 1300 K were measured. However, both methods converged to a mass loss rate of around 3.0 ± 0.1 mg/s as total energy deposition increased.

According to Figure 4, the machining orientation (parallel/perpendicular of main fibers' layers to the flow) yield different shapes of the composite article after testing. Parallel articles, Figure 4b, ablate cylindrically and more uniformly, whereas perpendicular articles ablate in a rather conical shape as shown in Figure 4c. These patterns are due to the machining orientation as they change axial and radial thermal conductivity between the two orientations. The parallel main fibers will allow heat to transport through the article streamwise, thus creating a more uniform temperature distribution and causing oxidation and ablation to occur uniformly throughout the entire article. This will dissipate the heat more efficiently streamwise down the test article. Perpendicular orientation of the main fibers will reduce radial thermal conductivity through the article, therefore causing the fibers hidden under the surface layers to be cooler and not ablate and oxidize at the same rate as the fibers at the surface. Additionally, heat needs to move through stacked layers of varying carbon fiber layers. Therefore, when new, the initial mass is $17{,}000 \pm 10$ mg and outer diameter at the thermocouple probe plane is 24.9 ± 0.1 mm for any orientation. However, that diameter shrinks, reducing to an average of 19.9 ± 0.1 mm for the parallel orientation, and 20.3 ± 0.1 mm for the perpendicular test article. This average was based off three articles of each type, after 3600 s of cumulative heat flux exposure and atmospheric air with temperatures beyond 800 K. Therefore, the axial recession rate of material was 1.7×10^{-3} mm/s for the parallel articles and 1.4×10^{-3} mm/s for perpendicular articles. For vacuum and hypersonic flow testing, the focus was primarily on the parallel article given the timeframe of the project.

The IR camera observations of the test article surface temperature allow the correlation of laser power, surface temperature and the rate of the test article mass loss, as is shown in Figures 5 and 6 for a single day of experimentation. Some data scattering is due to the test articles replacement (results differ slightly for newer vs. older test articles). Figure 5a demonstrates the test article steady state surface temperature acquired by the thermal camera versus the projected heat flux. The camera's proper readout starts from the surface temperature of 800 K. Two distinct ranges are considered: one for temperatures lower than 1400 K where the thermal radiation could be neglected, and one for temperatures greater than 1400 K where the thermal radiation is a major mechanism of the test article cooling. The data in Figure 5b excludes an initial preheating and indicates the mass loss rate at a given steady state surface temperature. Depending on the laser power, a noticeable test article recession is observed at temperatures greater than 1000 K. It gradually increases with the surface temperature magnitude within the range of the temperatures explored in this test series. Figure 6 plots mass loss rate against laser exposure time for maximum projected heat flux. This demonstrates that a steady state mass loss rate, dm/dt, greater than 3 mg/s is achieved for the maximum laser output power. For highly used test articles, this steady state mass loss rate of 3.0 mg/s was reached even earlier, at around 60 s of laser exposure time. A small uncertainty in the weighing of the test articles and in the startup and shutdown times of the laser is also accounted for in Figure 5b.

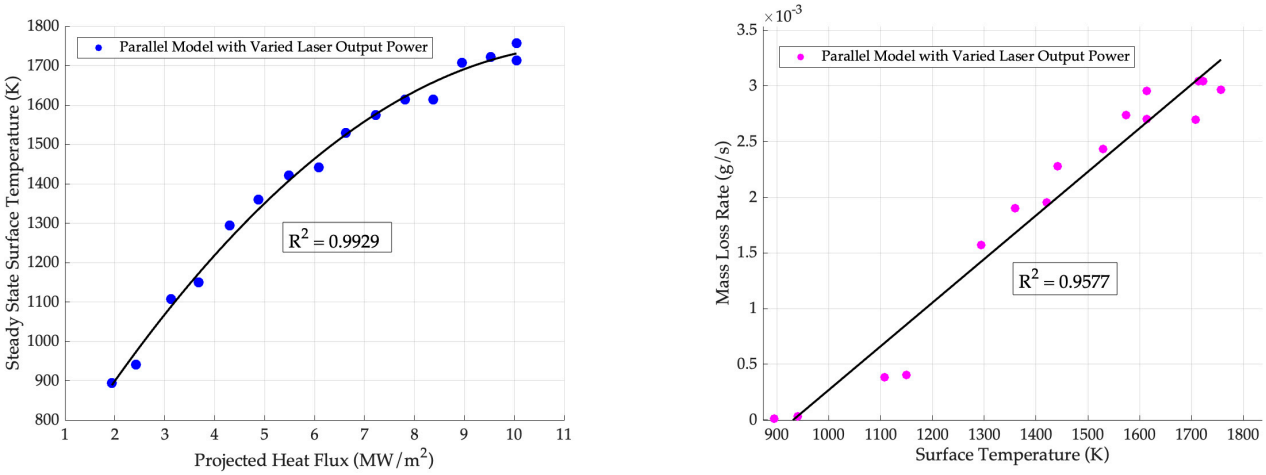

Figure 5. (**a**) Test article surface temperature versus laser power and (**b**) mass loss rate versus test article surface temperature.

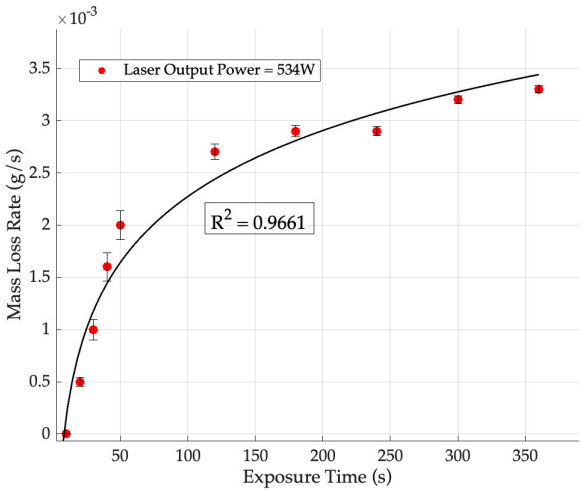

Figure 6. Mass loss rate versus laser exposure time at maximal power.

3.2. Mass Loss at Vacuum Conditions

Tests were also performed for the parallel articles under vacuum conditions at elevated temperatures. In these experiments, the parallel test articles were exposed to a heat flux provided by the laser for 6 min of exposure time at 9.4 MW/m^2. The test article experienced about 28 $\pm$ 0.1 mg of total mass loss. This corresponds to a negligibly low mass loss rate of around 0.08 mg/s compared to atmospheric and flow conditions. Regardless, it can be assumed that some percentage of mass loss under cold flow comes from thermal ablation. Likely, this mass loss is due to the thermal ablation of superheated fibers at the front of the test article or the vaporization of residual resin material from the laying out of carbon fibers.

3.3. Mass Loss Under Hypersonic Flow Conditions

The mass loss of the test article was experimentally determined under M = 6 flows of both air and nitrogen at flow stagnation temperature T_0 = 300 K. The hypersonic testing was performed at one single value of the laser power since there were several other variable parameters to consider. Each test run is time-consuming, which leads to a limited number of tests.

Shown in Table 1 are the results of multiple experiments performed under cold M = 6 flow with an article preheated by laser exposure at the radiative heat transfer of 9.4 MW/m^2.

As it was measured, the mass loss rate under cold hypersonic flow is significantly higher, approximately 40 times, than that under atmospheric conditions. As a note, increasing the stagnation pressure from 6.9 bar to 14 bar did not cause a substantial increase in the mass loss rate of the article. Further, when compared to a flow of nitrogen under similar surface temperature and mass flow rate conditions, the test article experienced a higher mass loss rate being exposed at airflow. This difference is suggested to be due to the oxidation reaction on the surface of the test article.

For the parallel articles, a comparison was made to observe the mass loss dynamics between the three testing conditions as shown by the diagram in Figure 7. In each test the article was exposed to a heat flux of 9.4 MW/m^2 for 360 s. The maximum surface temperature exceeded 2000 K. Note that the atmospheric testing with still air provides a reference point when compared to the vacuum and hypersonic flow at M = 6 of either air or nitrogen. Mass loss rate at atmospheric conditions was 3.28 $\pm$ 0.1 mg/s. For the vacuum, the mass loss was 0.08 $\pm$ 0.1 mg/s which is below the error of mass measurement and therefore negligible. This shows that there is no oxidation occurring in vacuum conditions. To ascertain a value for mass loss due purely to the flows of air or nitrogen, a mass loss of 28 mg due to laser erosion and thermal stress observed under vacuum conditions was assumed to be present in all tests and is compensated for in the relevant mass loss rate calculations. This leads to a mass loss rate under nitrogen flow of 31.2 mg/s. However, for newer test articles the total mass loss due to nitrogen flow testing was slightly lower, likely due to a smaller number of structural weaknesses. Given that for nitrogen flow there is no oxidation process, the ablation process dominates the mass loss dynamics, quantifying the mass loss rate due to pure mechanical flow erosion and ablation at 31.2 $\pm$ 0.1 mg/s. The mass loss rate under air flow was calculated to be 91.0 mg/s.

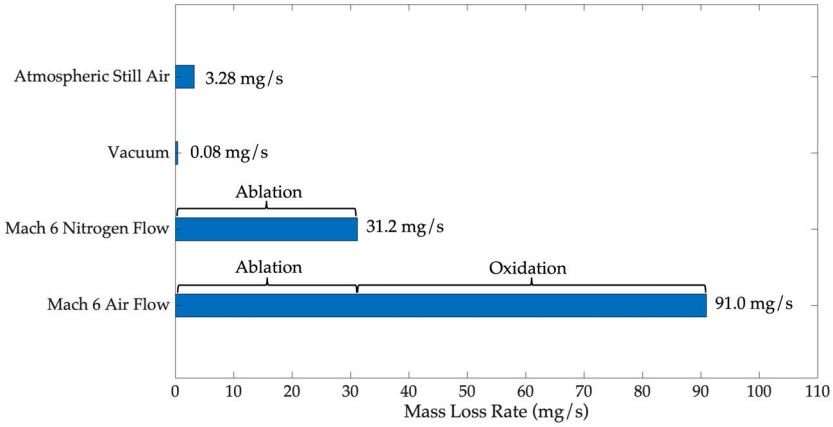

Figure 7. Mass loss rate comparison between the three testing conditions. For each test, the article was exposed to 9.4 MW/m^2 of heat flux for 360 s. For M = 6 flow, P_0 = 6.9 bar. The errors for each mass loss rate measurement were $\pm$0.1 mg/s.

The dynamics of the test article surface temperature are shown in Figure 8 for air flow, and in Figure 8b for N_2 flow. The time sequence of the flow run is as follows: the first 1.2 s is M = 6 flow (indicated in Figure 8a by a red bar), then about 0.5 s of supersonic unsteady flow, see Figure 12 for the details, and then about 0.6 s of weak subsonic flow of a remnant gas from the plenum section. There is a significant difference in the surface temperature dynamics between these two cases. The cooling rate observed under the flow of nitrogen was higher than that under flow of air. The hypothesis is that, likely, this is because the oxidation reaction is exothermic and releases additional heat on its own during the phases of both steady-state M = 6 flow and subsonic weak flow. Despite many uncertainties in chemical reactions details, a rough estimate of the chemical heat flux at

50 ± 0.1 mg/s of carbon oxidation returns a value well-above the 10 MW/m^2. During the phase of oscillating flow, the cooling rate is higher than the chemical reaction's contribution to the heat flux balance.

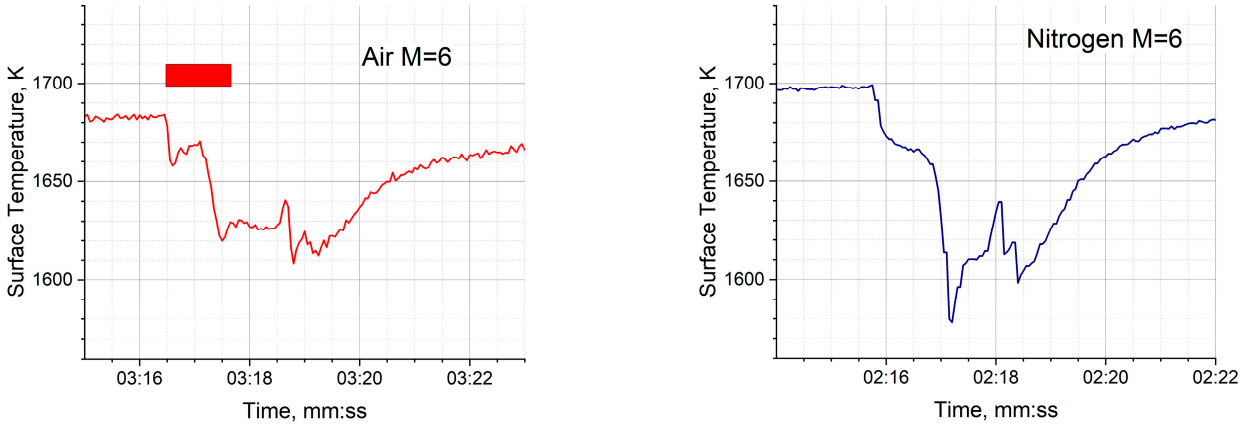

(**a**) (**b**)

Figure 8. Surface temperature dynamics during (**a**) M = 6 airflow and (**b**) M = 6 N_2 flow. The red bar indicates a duration of M = 6 flow.

4. Physical Mechanisms of C–C Composite Ablation

Live camera images of the heated article under atmospheric conditions reveal a rapid steady decrease in the size of superheated fibers at the front of the article, indicating intense oxidation. A comparison of the test article images is shown in Figure 9. Note the decrease in size of superheated fibers (lighter gray and white in color) moving from Figure 9a to d. The white and gray fibers shrink in size as exposure time increases. This is highlighted in the red circled regions in Figure 9b,c. The shrinkage of fibers forms a pit in the center of the front face, as evident in Figure 9a,d.

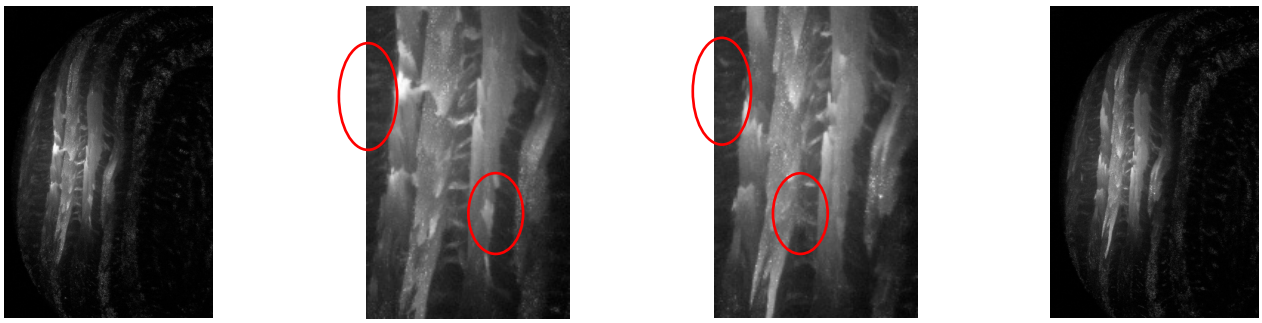

(**a**) (**b**) (**c**) (**d**)

Figure 9. (**a**) Article front surface before heat flux exposure; (**b**) zoomed-in image showing initial material recession areas; (**c**) zoomed-in image showing material recessed during the formation of the pit in the laser impingement spot; and (**d**) 360 s of laser exposure at atmospheric conditions.

Evident in high-framerate video footage of the article undergoing M = 6 flow of air is an increased rate of flaking of fibers. The process of flaking is shown in Figure 10 and occurs in the time span of 360 µs. The flaking is especially intense during the flow phase. Whereas the article under atmospheric conditions lost material due to the steady oxidation of fibers which led to the dissipation of the material on the microscale, M = 6 air flow causes rapid oxidation on the microscale with the added effect of mechanical shearing and breakage on the macroscale, which occurs on the scale of microseconds throughout the duration of flow. Additionally, flaking occurs sporadically throughout the entire time span of the flow. This

indicates that simple mechanical breakage is not the only mechanism of destruction. As the first air molecules reach the article, fibers that were structurally weak due to manufacturing imperfections or prior testing are blown out immediately. Stronger fibers will undergo oxidation, forming oxidation pits, which lead to more structural weaknesses. As the wave of air continues blowing, these created structural weaknesses lead to the breakage of even more fibers, as indicated by the continued flaking of fibers after the initial wave of air. To confirm this, the heated test article was tested under a flow of N_2, where a lower mass loss rate was observed, as shown in Figure 6. High-framerate video footage of the test article under N_2 flow reveals a rapid blowing out of small filaments at the beginning of the flow. This is shown in Figure 11. The photos have been edited to help visualize the small superheated white fibers leaving the surface directly in front of the test article. This process occurs during the very first milliseconds of flow and finishes about a quarter of a second into flow. Throughout the rest of the flow, occasional flaking of superheated fibers occurs, but at a substantially lower rate when compared to video footage of the test article under airflow. Additionally, the observed size of flakes breaking off the test article were smaller when compared to the test article under air flow. This leads to the conclusion that for a moderately used test article, about one third of the mass loss rate can be attributed to the mechanical blowing out of weakened fibers and two thirds of the mass loss rate can be attributed to the rapid oxidation and destruction of strong fibers. For a new, unused test article, it was observed that the mechanical breakage of fibers contributes to a slightly smaller portion of the overall mass loss rate, likely due to the lower number of structural weaknesses.

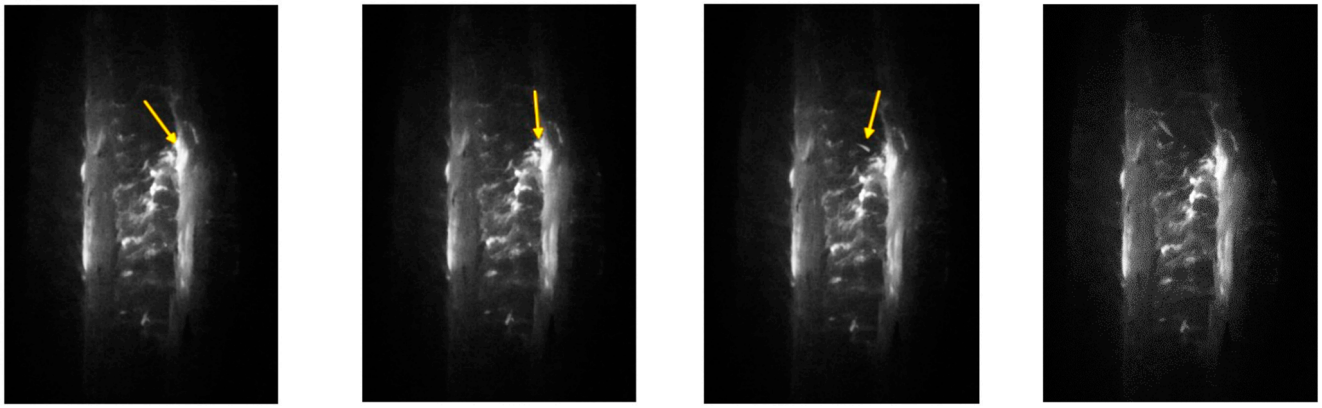

Figure 10. Flaking mechanism of superheated fibers on the surface of the parallel test article, arrows indicating flakes moving during flow. Each image shows flakes removed from the surface at different time instances, (**a**) t_1, (**b**) $t_2 > t_1$, (**c**) $t_3 > t_2$, and (**d**) $t_4 > t_3$.

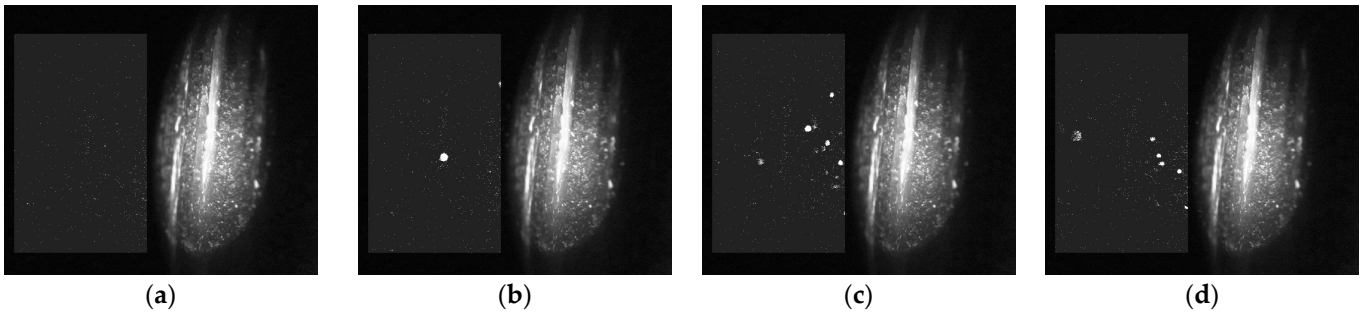

Figure 11. Blowout mechanism of small, weakened fibers on the surface of the parallel test article under a M = 6 flow of nitrogen. (**a**) t_1, (**b**) $t_2 > t_1$, (**c**) $t_3 > t_2$, and (**d**) $t_4 > t_3$.

The mechanical destruction of the overheated individual carbon filaments is likely to be caused by a high-speed flow blowout. However, hypothetically, it might be significantly intensified as the bow shock wave instability resulted in pressure oscillations in the compression area of the blunt body. A comparison of instant schlieren images of a steady flow over the heated test article with a strongly oscillating flow is shown in Figure 12.

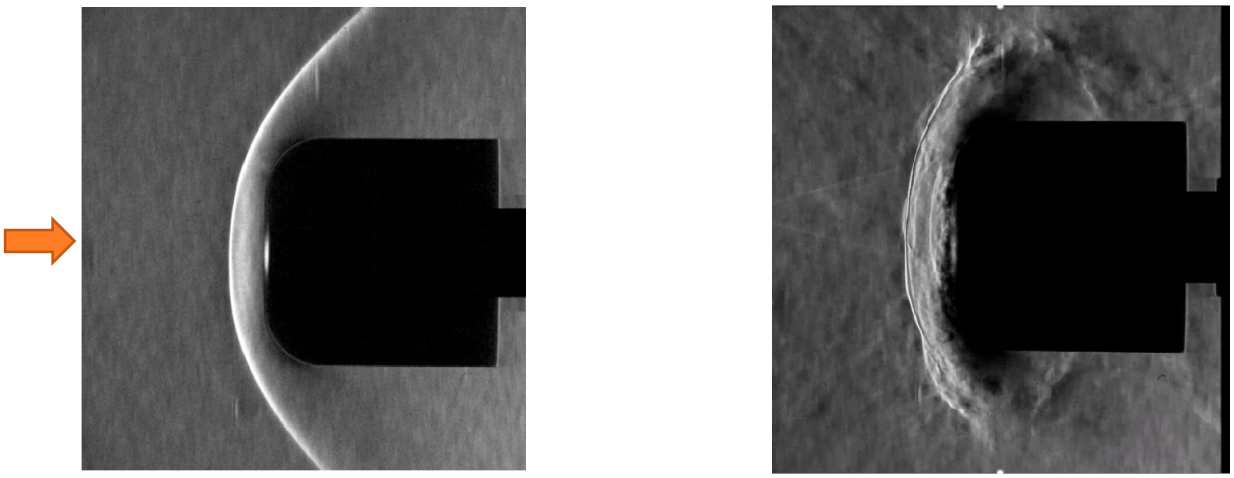

(**a**) (**b**)

Figure 12. (**a**) Schlieren images of steady bow shock wave with arrow showing direction of the flow and (**b**) one under oscillating mode.

To explore the physical details of fiber destruction, images were taken to examine the microstructure of the test article surface after ablation and oxidation using scanning electron microscopy. Figure 13 shows a group of fibers on the test article surface for various testing conditions. As seen in Figure 13, many small pits are visible on both the internal solid carbon fiber and sheathing CVI carbon material. There are likely two reasons for the existence of these pits. Firstly, the smalls pits on the CVI carbon are evident in all test articles. In quantity, they are least prevalent in the test article tested under vacuum conditions and are smaller in size as well. Likely, imperfections in the process of chemical vapor infiltration leads to the initial creation of these pits. The pits could be enlarged by the vaporization of leftover resin material from the laying out of carbon fibers, or from thermal stresses caused by the laser preheating. These pits are also evident on the test article that underwent N_2 flow, indicating that at elevated temperatures this material likely weakens and is mechanically blown out in sections by the flow. As evident in Figure 13c, much of this CVI carbon matrix is missing, with sharp-shaped fibers left behind. Likely, this is the material that is weakened and mechanically blown out by the flow first. Lastly, the oxidation pits on the CVI carbon matrix are large and plentiful on both the test article that was heated under atmospheric conditions and under M = 6 air flow. Therefore, it is noted that these pits are local regions where oxidation occurs and causes structural weaknesses. The structural failures of the CVI carbon matrix are seen where there are gaps in the structure. This structural failure occurs even without flow, as seen in the gaps in the structure in Figure 13a.

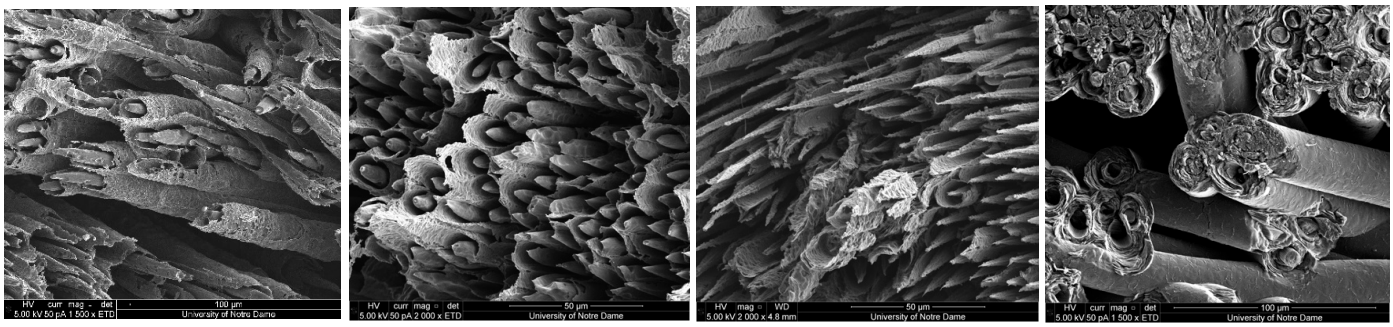

(**a**) (**b**) (**c**) (**d**)

Figure 13. Fiber bundle on article surface after laser exposure during: (**a**) atmospheric conditions; (**b**) M = 6 airflow; (**c**) M = 6 nitrogen flow; and (**d**) vacuum conditions.

Figure 14 shows a single fiber on the surface for each tested article. As seen in Figures 13a and 14a, the test article heated under atmospheric conditions has carbon fibers with many oxidation pits. These are also evident by observing the images of the test article that underwent the M = 6 flow of air, seen in Figures 13b and 14b. Note the relative smoothness of the test articles that were heated in the presence of oxygen, Figure 14a,b, when compared to the test articles heated without oxygen present, Figure 14c,d. Likely, the oxygen present around the test article will oxidize the small imperfections around the edge of the internal fiber first, leading to a smoother surface, but still a pointy morphology of the fiber, which agrees with [24]. Then, small pits will form on the fiber where more oxidation takes place, creating voids as described by [25], either due to elevated temperature, structural weakness, or as [26] states, that oxygen diffuses at that specific location. Also of note is the sharpness of the fibers. The fibers on the test article that underwent nitrogen flow are sharper than the fibers on the other test articles. The flow itself appears to have decreased the radial size of the fiber through mechanical abrasion and sheared away the edges on the fibers of the test article that underwent nitrogen flow, rather than corrode and smooth the surface like the process of oxidation does. This process of mechanical abrasion and edge-shearing is also present on the test article that underwent the flow of air, given that the fibers form sharper points than the test article heated under atmospheric conditions. However, these processes are occurring simultaneously with the smoothing-out mechanism of oxidation, leading to points not as sharp as those under nitrogen flow.

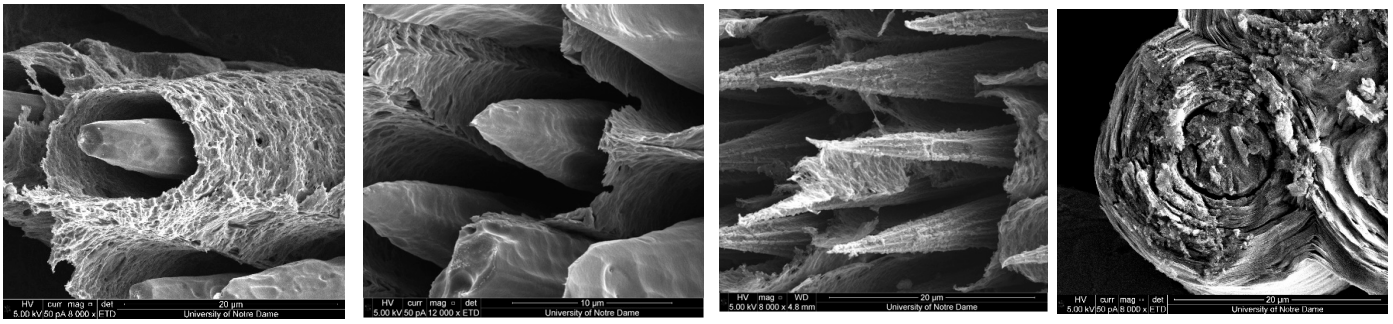

(**a**) (**b**) (**c**) (**d**)

Figure 14. Individual fiber on the article surface after laser exposure during: (**a**) atmospheric conditions; (**b**) M = 6 airflow; (**c**) M = 6 nitrogen flow; and (**d**) vacuum conditions.

Figures 13d and 14d shows the surface structure after the test article is exposed to laser heating under vacuum conditions and no flow: the surface structure is not different when compared to the initial surface structure after the machining of the test article. Still,

note the initial imperfections in the material caused by machining and imperfections in the CVI process.

5. Discussion and Conclusions

Designing vehicles capable of withstanding the harsh conditions exhibited during hypersonic flight is a rather difficult problem to tackle. Specifically, dealing with the high heat flux generated at the leading edges of the vehicle and in the engine is key for the survival of the vehicle. According to available publications [5,23] related to existing and prospective thermal protection systems, conventional materials may prove to be ready for applications [9], but they have limited capabilities in terms of withstanding their maximum surface temperature and their survivability in the harsh environment during hypersonic flight. For thermal protection systems of hypersonic vehicles, materials such as C–C composites may be a reasonable selection thanks to the capacity of maintaining high mechanical strength at temperatures greater than 2000 K [2,26]. However, lower cost of the materials fabrication, reduction in the physical parameters' uncertainties, and a detailed physical model of the material's interaction with high-enthalpy flows are still of high demand.

A combination of ground testing to study the phenomena, computational modeling, and flight testing is a proper pathway to routine practical implementation. The ground testing can simulate the harsh environment relevant to hypersonic flight and allows the collection of a basic dataset to characterize material properties and the details of behavior on macro and micro scales. In this work, the commercial C–C composite material was tested under high thermal flux, causing a steady state surface temperature up to 2000 K at variable conditions, including open atmosphere, vacuum, and high-speed flows of both air and nitrogen.

This testing allowed for the accurate and consistent measurement of material mass loss rates due to thermal ablation and oxidation. These processes are explained qualitatively through the analysis of scanning electron microscopy images and high-framerate live videos. Quantitatively, these processes were characterized through mass tracking and surface and internal temperatures measurements. High-framerate images taken during M = 6 flow testing provided insights on how superheated small flakes mechanically broke from the article, showing evidence of ablation thus leading to rapid destruction of the material. Scanning electron microscopy images revealed that, under quiescent atmospheric air at high temperature, the sheathing material surrounding the individual carbon fibers exhibited a rough surface, with numerous pits created by the oxidation process. Under hypersonic air flow, in which oxidation and ablation are present, the morphology of the material was observed to be pointy and that the carbon fiber was oxidizing slower than the sheathing material, which qualitatively agrees with the results found by other authors [24]. However, the microscopic images for the article that was tested under hypersonic nitrogen flow exhibited a different behavior. The exposed fibers are shaped into pointy forms, sharper compared to the ones exposed to air flow, indicating the effect of accelerated oxidation. This shows that, under nitrogen flow, the mechanical erosion in combination with thermal stresses induced by the high thermal gradient weaken the structure of the carbon fiber, creating an abrasive effect eroding the fibers.

The main contributor to the material mass loss process was determined to be oxidation, followed by the combined thermal ablation and mechanical breakage of the fibers due to flow mechanical stress. The results of the ground testing of the test article with dimensions $d \times x = 25.4 \times 25.4$ mm show that the mass loss rate of C–C composites in M = 6 flow was up to 91.0 ± 0.1 mg/s for air flow at temperatures exceeding 1300 K. Keeping in mind the front surface area S of the test article, these numbers correspond to the mass loss

flux $(1/S)(\partial m/\partial t > 0.2\ kg/m^2s)$, or the material linear decrease $\partial x/\partial t > 0.1$ mm/s. Under a M = 6 flow of nitrogen, the mass loss rate was measured as high as 31.2 ± 0.1 mg/s. Under air flow, the intense oxidation process increases the mass loss rate compared to that under nitrogen flow. Under a M = 6 flow of air, about two thirds of the mass loss rate can be attributed to the effects of oxidation. Under nitrogen flow the recession occurs due to thermal/mechanical ablation and additional structural weakening of the fibers. For reference, in atmospheric quiescent air, the mass loss was around 3.0 ± 0.1 mg/s for the same heat flux exposure. Under vacuum conditions and identical heat flux exposure, testing proved that a very small to negligible thermal ablation occurs (<0.1 mg/s) with no oxidation.

The study concluded that the destruction mechanism of C–C composite materials under high-speed airflow differs significantly from one under stagnant conditions. As a result, there was an increase of about 1.5 orders of magnitude in the rate of material destruction. As part of the ongoing study, results from the uncoated C–C composites will be compared to those from coated articles, including their oxidation rate and thermal shock resistance. Future work will include data processing refinement to improve the graphing visualization, and more vacuum and hypersonic flow testing. Thermal and mechanical stresses will also be examined in the degradation of mechanical properties and the recession of composite materials.

Author Contributions: Each author contributed to the work on this research in multiple ways as follows. Conceptualization, S.B.L. and R.G.; methodology, A.I.S. and R.B.; formal analysis A.I.S. and R.B.; investigation, A.I.S., R.B. and S.B.L.; resources, S.B.L.; data curation S.B.L.; writing—original draft preparation, R.B.; writing—review and editing, A.I.S., S.B.L. and R.G.; visualization, R.B.; supervision S.B.L. and R.G.; funding acquisition, S.B.L. All authors have read and agreed to the published version of the manuscript.

Funding: This research was funded by the US Air Force Office of Scientific Research (PM Dr. Fariba Fahroo), grant number FA9550-22-1-0065.

Data Availability Statement: Due to privacy restrictions, data used for the evaluation and creation of the results presented in this manuscript remain unavailable for public access. However, some data related to specific measurements could be shared on demand.

Acknowledgments: Three-directional needled felt PAN-based carbon fiber reinforced carbon matrix commercial composites were kindly provided by Honeywell Aircraft Landing Systems. The authors are grateful to Philip Lax for his help in schlieren visualization. The authors would also like to thank Tatyana Orlova at the Notre Dame Integrated Imaging Facility for guiding the electron microscopy visualization of the exposed articles.

Conflicts of Interest: The author Richard Gulotty is employed by the company Honeywell International Inc. The remaining authors declare that the research was conducted in the absence of any commercial or financial relationships that could be construed as a potential conflict of interest. The material presented in this work was reviewed by Honeywell Aircraft Landing Systems and approved for publication.

References

1. Van Wie, D.M. Hypersonics: Past Present, and Potential Future. *Johns Hopkins APL Tech. Dig.* **2021**, *35*, 335–341.
2. Glass, D.E. Thermal Protection Systems and Hot Structures for Hypersonic Vehicles. In *Aerospace Materials and Applications*; American Institute of Aeronautics and Astronautics: Reston, VA, USA, 2018; pp. 531–578.
3. Tenney, D.R.; Lisagor, W.B.; Dixon, S.C. Materials and structures for hypersonic vehicles. *J. Aircr.* **1989**, *26*, 953–970. [CrossRef]
4. Zhang, S.; Li, X.; Zuo, J.; Qin, J.; Cheng, K.; Feng, Y.; Bao, W. Research progress on active thermal protection for hypersonic vehicles. *Prog. Aerosp. Sci.* **2020**, *119*, 100646. [CrossRef]
5. Peters, A.B.; Zhang, D.; Chen, S.; Ott, C.; Oses, C.; Curtarolo, S.; McCue, I.; Pollock, T.M.; Prameela, S.E. Materials design for hypersonics. *Nat. Commun.* **2024**, *15*, 3328. [CrossRef] [PubMed]

6. Zhu, T.; Wang, Z. Advances in processing and ablation properties of carbon fiber reinforced ultra-high temperature ceramic composites. *Rev. Adv. Mater. Sci.* **2024**, *63*, 20240029. [CrossRef]
7. Ohlhorst, C.W.; Glass, D.E.; Bruce, W.E.; Lindell, M.C.; Vaughn, W.L.; Dirling, R.B.; Hogenson, P.A.; Nichols, J.M.; Risner, N.W.; Thompson, D.R. Development of X-43-A Mach 10 Leading Edge. In Proceedings of the 56th International Astronautical Congress in 2005, Fukuoka, Japan, 16–21 October 2005.
8. Glass, D. Physical Challenges and Limitations Confronting the Use of UHTCs on Hypersonic Vehicles. In Proceedings of the 17th AIAA International Space Planes and Hypersonic Systems and Technologies Conference, Santa Clara, CA, USA, 11–14 April 2011; pp. 2011–2304.
9. Fahrenholtz, W.G.; Hilmas, G.E. Ultra-high temperature ceramics: Materials for extreme environment. *Scr. Mater.* **2017**, *129*, 94–99. [CrossRef]
10. Windhorst, T.; Blount, G. Carbon-carbon composites: A summary of recent developments and applications. *Mater. Des.* **1997**, *18*, 11–15. [CrossRef]
11. Ohlhorst, C.W.; Vaughn, W.L.; Ransone, P.O.; Tsou, H.-T. *Thermal Conductivity Database of Various Structural Carbon-Carbon Composite Materials*; NASA: Linthicum Heights, MD, USA; NTIS: Springfield, VA, USA, 1997.
12. Barrios-Lobelle, A.; Davuluri, R.; Fu, R.; Martin, A.; Poovathingal, S.J. Surface Oxidation of Carbon/Carbon Composites in Hypersonic Environments. In Proceedings of the AIAA Scitech 2021 Forum, Online, 11–15,19–21 January 2021.
13. Keswani, S.T.; Kuo, K.K. Validation of an Aerothermochemical Model for Graphite Nozzle Recession and Heat-Transfer Processes. *Combust. Sci. Technol.* **1986**, *47*, 177–192. [CrossRef]
14. Borie, V.; Brulard, J.; Lengelle, G. Aerothermochemical Analysis of Carbon-Carbon Nozzle Regression in Solid-Propellant Rocket Motors. *J. Propuls. Power* **1989**, *5*, 665–673. [CrossRef]
15. Thakre, P.; Yang, V. Chemical Erosion of Carbon–Carbon/Graphite Nozzles in Solid-Propellant Rocket Motors. *J. Propuls. Power* **2008**, *24*, 822–833. [CrossRef]
16. Panerai, F.; Cochell, T.; Martin, A.; White, J.D. Experimental measurements of the high-temperature oxidation of carbon fibers. *Int. J. Heat Mass Transf.* **2019**, *136*, 972–986. [CrossRef]
17. Ge, H.; Zhang, L.; Zhang, H.; Wang, F.; Gao, X.; Song, Y. Cyclic Ablation Properties of C/SiC-ZrC Composites. *Aerospace* **2024**, *11*, 432. [CrossRef]
18. Zhou, W.; Xiao, P.; Luo, W.; Li, Y. Microstructural evolution of SiC coating on C/C composites exposed to 1500 °C in ambient air. *Ceram. Int.* **2019**, *45*, 854–860. [CrossRef]
19. Marshall, L.A.; Bahm, C.; Corpening, G.; Sherrill, R. Overview With Results and Lessons Learned of the X-43A Mach 10 Flight. In Proceedings of the AIAA Scitech Forum, Capua, Italy, 16–20 May 2005; pp. 1–23.
20. Slobodkin, L.S.; Flyaks, M.Y. Emissivity measurement for a carbon-carbon composite and a phenolic carbon plastic. *J. Eng. Phys.* **1989**, *57*, 972–975. [CrossRef]
21. Sun, X.; Yang, H.; Mi, T. Heat Transfer and Ablation Prediction of Carbon/Carbon Composites in a Hypersonic Environment Using Fluid-Thermal-Ablation Multiphysical Coupling. *Int. J. Aerosp. Eng.* **2020**, *2020*, 9232684. [CrossRef]
22. Zhang, J. Oxidation Protection of Carbon/Carbon Composites and Non-Destructive Characterization Methodology Development. Ph.D. Thesis, Sorbonne University, Paris, French, 2019.
23. Bertin, J.J.; Cummings, R.M. Fifty years of hypersonics: Where we've been, where we're going. *Prog. Aerosp. Sci.* **2003**, *39*, 511–536. [CrossRef]
24. Farhan, S.; UI-Haq, N.; Kuo, W.-S. Degradation behavior of 4D carbon/carbon composites under supersonic oxidative air plasma. *Ceram. Int.* **2013**, *39*, 7135–7142. [CrossRef]
25. Jacobson, N.; Curry, D. Oxidation Microstructure Studies of Reinforced Carbon/Carbon. *Carbon* **2006**, *44*, 1142–1150. [CrossRef]
26. Han, M.; Zhou, C.; Sillberschmidt, V.; Bi, Q. Oxidation behaviour and residual mechanical properties of carbon/carbon composites. *Carbon Lett.* **2023**, *33*, 1241–1252. [CrossRef]
27. Fradin, M.; Vignolis, G.; Rebillat, F.; Haras, K.; Gregis, C. Oxidation behavior of nozzle throat carbon/carbon composites featuring variable densities. In Proceedings of the 9th European Conference for Aeronautics and Space Sciences, Lille, France, 27 June–1 July 2022; pp. 1–10.
28. Ozcan, S.; Filip, P. Wear of carbon fiber reinforced carbon matrix composites: Study of abrasive, oxidative wear and influence of humidity. *Carbon* **2013**, *62*, 240–247. [CrossRef]
29. Ozcan, S.; Tezcan, J.; Filip, P. Microstructure and elastic properties of individual components of C/C composites. *Carbon* **2009**, *47*, 3403–3514. [CrossRef]